

Iron dissolution and speciation from combustion particles under environmentally relevant conditions

Cecily Szady^A , Grace Picarillo^A , Emily J. Davis^A , Donata Drapanauskaite^{B,C}, Kristina Buneviciene^{B,C}, Jonas Baltrusaitis^B  and Juan G. Navea^{A,*} 

Environmental context. Iron-containing combustion particles are likely to contribute to environmental iron deposition, while atmospheric acidic processing of such particles can promote their dissolution. Here we report the surface-mediated dissolution of iron from ashes generated by biomass burning power plants and kilns. Examination of the dissolution process at several environmentally relevant pHs, suggests that pH has little impact on the fraction of bioavailable Fe(II) that dissolves into the aqueous phase, although Fe(III) is heavily pH dependent.

For full list of author affiliations and declarations see end of paper

***Correspondence to:**

Juan G. Navea
Chemistry Department, Skidmore College,
Saratoga Springs, NY 12866-1632, USA
Email: jnavea@skidmore.edu

Handling Editor:

Zongbo Shi

Received: 15 March 2023

Accepted: 17 July 2023

Published: 8 August 2023

Cite this:

Szady C *et al.* (2023)
Environmental Chemistry
20(4), 171–182. doi:10.1071/EN23022

© 2023 The Author(s) (or their employer(s)). Published by CSIRO Publishing.

This is an open access article distributed under the Creative Commons Attribution-NonCommercial-NoDerivatives 4.0 International License (CC BY-NC-ND)

OPEN ACCESS

ABSTRACT

Rationale. Anthropogenic combustion particles, such as ash produced in power plants or kilns, are byproducts with limited use that accumulate in large deposits and become materials of environmental concern. While stored, these particles can be carried by winds into the atmosphere or into soil or near water bodies. Recent studies suggest that a fraction of metals present in the environment come from combustion particles. **Methodology.** In this study, we carry out a comparative study of iron dissolution and speciation from two different combustion particles: bottom ash from a biomass-fired power plant (BA) and lime kiln dust (LKD). Samples were fully characterised and their iron leaching was investigated in aqueous suspensions under environmentally relevant acidic conditions. Iron analysis and speciation was carried out calorimetrically. **Results.** For the combustion particles examined, the fraction of bioavailable Fe²⁺ is lower than Fe³⁺. The solubility of Fe³⁺ is highly dependent on pH, dropping significantly at pHs higher than 3. On the other hand, the solubility of Fe²⁺ from both BA and LKD was found to be relatively constant over the range of pH investigated. **Discussion.** Iron availability from combustion particles with similar mineralogy is driven by the particle's surface properties. While iron from LKD dissolves faster than that from BA, the initial rate of dissolution of iron remains statistically constant at pHs relevant for the atmospheric aerosol deliquescent layer, decreasing at pHs above 3. This work provides insight into the ability of combustion particles to provide iron micronutrients under different environmentally relevant acidic conditions.

Keywords: acidic processing, atmospheric chemistry, bioavailability, biogeochemistry, combustion particles, iron dissolution, speciation.

Introduction

Iron is an essential environmental micronutrient as it participates in crucial biogeochemical processes, such as oxygen transport and oxidation–reduction reactions (Rubasinghe *et al.* 2010; Hettiarachchi *et al.* 2018a; Hettiarachchi *et al.* 2018b; Hettiarachchi *et al.* 2019). Recent experimental and modelling work suggests that, over the last two decades, anthropogenic particles have significantly contributed to an increase in iron deposition flux (Matsui *et al.* 2018). The major source of anthropogenic aerosols are combustion processes, mainly the burning of fossil fuels and biomass. These particles have a wide range of iron concentrations, ranging from 5 to 17 000 ng m⁻³ (Hettiarachchi *et al.* 2018a; Matsui *et al.* 2018). Thus, an increase in combustion particle emissions leads to an increase in anthropogenic environmental iron driven by the

atmospheric transport of ashes and other combustion particles (Ramanathan et al. 2001; Ojha et al. 2004; Haque 2013; Matsui et al. 2018). While combustion particles only account for <5% of the world's aerosols, their small size and long atmospheric lifetime result in an estimated contribution of up to 50% of the global iron, with up to 30% of total iron deposited in the ocean (Moore et al. 2001; Chuang et al. 2005; Chen et al. 2006; Luo et al. 2008; Hettiarachchi et al. 2018a; Pinedo-González et al. 2020).

Either through direct emission or through efforts to use or dispose of combustion byproducts, these combustion particles can result in heavy metal transfer into environmental water (Nowinski et al. 2012; Mueller et al. 2013). While combustion particles have little utility and usually accumulate in deposits or escape into the immediate surroundings, recent efforts aspire to repurpose them in water remediation and soil applications, thus increasing their presence in the environment (Drapanauskaitė et al. 2022). Combustion particles have been shown to undergo acidic processing once they are transported and partitioned into the atmosphere, where the highly acidic aerosol deliquescent layer leaches iron and other heavy metals (Navea and Grassian 2017; Marcotte et al. 2020; Leonardi et al. 2020). Recent work shows that the rate of iron dissolution due to atmospheric acidic processing from combustion particles is faster than that observed from mineral dust (Schroth et al. 2009; Chen et al. 2012; Borchering et al. 2013; Al-Abadleh 2015; Borgatta and Navea 2015; Borgatta et al. 2016; Hettiarachchi et al. 2019; Hettiarachchi and Rubasinghege 2020; Kim et al. 2020). To a lesser extent, this acidic processing of combustion particles has also been proposed for polluted underground water and acidic soil (Basu et al. 2009; Koshy and Singh 2016; Chowdhury et al. 2022). These studies have shown that the ability of combustion particles to mobilise iron into an environmental matrix depends highly on the pH of the media and the mineralogy of the particles. The high variability in mineralogy, combustion process, and matrix acidity leads to large uncertainties in our current understanding of iron dissolution from anthropogenic combustion particles. This iron leaching has been linked to phytoplankton blooms in the marine boundary layer and the emergence of plankton in freshwater bodies (Mahowald et al. 2009; Hettiarachchi et al. 2018a; Hettiarachchi et al. 2018b; Al-Abadleh 2021; Al-Abadleh et al. 2022). The ability of iron-bearing combustion particles to induce biological activity can increase carbon export in the world's oceans by one-third (Moore et al. 2001, 2013). Thus, anthropogenic sources of iron have significant importance as an environmental nutrient and climate control factor (Pinedo-González et al. 2020). Yet, iron dissolution from anthropogenic aerosols is a complex and not fully understood process.

Recent work shows that iron leaching from combustion particles varies depending on the source, the environmental conditions, and the combustion completeness of the particles (Chen and Grassian 2013; Borgatta et al. 2016; Kim et al. 2020). Here, we present a study on the dissolution and

mobility of iron from particles combusted in different processes: lime kiln dust (LKD) and biomass combustion bottom ash (BA). Similar to mineral dust or particles of anthropogenic origin, these combustion particles can partition into the atmosphere, carried from fields by winds, with important environmental implications. The combustion samples investigated here represent increasingly relevant iron-containing byproducts, with worldwide thermochemical processing of biomass generating an estimated 480 million tons of ashes annually (Vassilev et al. 2013), while 2.5 million metric tons of LKD are produced annually in the United States alone (Arulrajah et al. 2017). The environmental impact of these anthropogenic particles is becoming increasingly important, as storage of these byproducts becomes more challenging and their use more widespread (Luo et al. 2008). Thus, comparing the yields of iron species leached out of combustions particles is crucial for understanding the effect of iron in different biogeochemical cycles.

Experimental

Material sources

BA was obtained from SC 'Akmenės Energija', Venta, Lithuania, where mixed biomass waste was used as fuel. LKD was obtained from JSC Naujasis Kalcitas, Naujoji Akmenė, Lithuania. Samples were collected from the top of the ash pile. To avoid any large fractions of residual non-combusted biomass or partially combusted char, samples were initially processed for the laboratory experiments by sieving through a 0.063-mm mesh sieve. Bulk metal composition analysis of the combustion powder samples was carried out using X-ray fluorescence (XRF) employing a Bruker Tracer III SD spectrometer. Accurate measurement of total iron content in BA and LKD was carried out via atomic absorption spectroscopy (AAS) using a PerkinElmer AAnalyst 800 spectrometer; approximately 0.1 g of combustion samples were acid digested in a mixture of 5 mL HNO₃ and 3 mL H₂O₂ (Borgatta et al. 2016; Kim et al. 2020) for analysis. The mineralogy of the samples was investigated using X-ray diffraction (XRD, Rigaku) and infrared spectroscopy (FTIR, Perkin Elmer). Vibrational scans were collected with a single beam Perkin-Elmer FTIR spectrometer, equipped with a ZnSe ATR element and a DLaTGS/KBr detector. Typically, samples were vacuum dried overnight at 373 K before analysis with 100 scans averaged at a resolution of 4 cm⁻¹ over the full spectroscopic range extending from 800 to 4000 cm⁻¹.

X-Ray photoelectron spectroscopy (XPS) spectra of the BA and LKD surface were collected with a SPECS Near Atmospheric Pressure X-ray Photoelectron Spectroscopy (NAP-XPS) system. The NAP-XPS system was equipped with an XR 50 MF Al K α X-ray source with a μ -FOCUS 600 X-ray monochromator. Al K α radiation was used with an X-ray beam energy of 1486.7 eV and power of 120 W.

A PHOIBOS NAP *in situ* 1D-DLD hemispherical electron energy analyser (~ 0.85 eV energy resolution and 1 mm entrance aperture) collected the spectra. The pressure during the entire NAP-XPS experiment was always kept at $\sim 10^{-8}$ mbar. A pass energy of 100 eV was utilised for survey spectra and 20 eV for high-resolution spectra. Data were processed using Casa XPS software (Fairley *et al.* 2021). Finally, the surface areas for all combustion samples were determined using an eleven-point N_2 -BET adsorption isotherm, acquired with a Quantachrome Nova 1200 surface area analyser. The samples were dried under vacuum overnight before the surface area measurement.

Dissolution experiments

The acidic processing of the combustion particles was simulated in a 300 mL custom-built jacketed beaker with an airtight top at 298 K (Borgatta *et al.* 2016; Kim *et al.* 2020). Dissolution of iron and speciation analysis were performed on suspensions of 1 g L^{-1} of the combustion particles in constantly stirred solutions acidified with hydrochloric acid. As discussed before, the acid deliquescence layer that mobilises iron from combustion particles during atmospheric transport can reach pH values between 1 and 4 (Usher *et al.* 2003), with a pH of around 4 also representing the extreme acidity in polluted ash ponds (Kabisch and Hemmerling 1982). Thus, in the suspension experiments the pH was controlled at 1.0 ± 0.1 , 2.0 ± 0.1 , 3.0 ± 0.1 , and 4.0 ± 0.1 . The pH was kept constant by adding microliters of concentrated HCl when needed with negligible changes in volume and concentration of dissolved iron. In a typical experiment, aliquots were periodically taken from the reaction vessel and filtered through $0.2 \mu\text{m}$ pore size polytetrafluoroethylene filters (PTEE) for iron analysis. Although most available iron partitions to the aqueous phase within the first 300 min, all suspension experiments were carried out for a minimum of 50 h to ensure that equilibrium had been reached.

To prevent oxidation of Fe^{2+} by dissolved oxygen once leached from the combustion samples, all dissolution experiments were carried out in an oxygen-free atmosphere achieved with a continuous flow of 5 sccm of nitrogen above the solution surface (Borgatta *et al.* 2016; Kim *et al.* 2020). Before the suspension experiment, the acidic solution was deoxygenated by bubbling nitrogen for 15 min. This oxygen-free environment allowed for a better quantification of both Fe^{3+} and Fe^{2+} leached from the combustion

samples during the suspension experiments. In addition, to control the variations in ionic strength in the suspension solution as the dissolution takes place, all acidic solutions were adjusted to 1.0 M NaCl ensuring a constant ionic strength all through the experimental time. Iron speciation and quantification started at the moment of sample loading into the acid solution, defined as $t = 0$ min. As reported in previous work, dissolved iron species were quantified using 1,10-phenanthroline, which forms an orange complex with Fe^{2+} with an absorbance band at 510 nm (Borgatta and Navea 2015; Borgatta *et al.* 2016; Kim *et al.* 2020). Total dissolved iron was quantified in the same samples by adding hydroxylamine to reduce all Fe^{3+} to Fe^{2+} before phenanthroline complexation. The absorbance measured via the colorimetric method was converted into concentrations using aqueous standards prepared from anhydrous ferrous chloride (Sigma-Aldrich). All colorimetric measurements were performed in triplicate using a Lambda 35 Perkin-Elmer UV/Vis spectrophotometer.

Results and discussion

Characterisation of combustion samples

Table 1 shows the major elements detected via XRF. Overall, the bulk iron in LKD and BA was determined to be 14.9 ± 0.8 and $12.4 \pm 0.5 \text{ mg g}^{-1}$, respectively. While iron content in both samples is relatively similar, it is comparatively low with respect of fly ash samples examined in previous work (Navea *et al.* 2010; Borgatta *et al.* 2016; Kim *et al.* 2020).

In Fig. 1, the XRD patterns show structural and compositional similarities between the two samples. Both LKD and BA show a fraction of mullite ($3\text{Al}_2\text{O}_3 \cdot 2\text{SiO}_2$), typically formed during the combustion of aluminosilicate components in fuels (Navea *et al.* 2010; Borgatta *et al.* 2016; Kim *et al.* 2020; Drapanauskaite *et al.* 2021). In addition, diffraction patterns due to the presence of calcium feldspars, quartz (SiO_2), and traces of hematite (Fe_2O_3) and magnetite (Fe_3O_4) can be observed. Finally, a clear diffraction pattern for calcite (CaCO_3) is observed in both samples. Full combustion, observed in samples collected in power plant stacks or emitted directly into the atmosphere (Navea *et al.* 2010; Borgatta *et al.* 2016; Kim *et al.* 2020), convert all calcite into calcium oxide, removing carbonate and bicarbonate minerals from the sample. The presence of carbonate minerals in

Table 1. X-Ray fluorescence spectroscopy (XRF) results for LKD and BA in percent composition.

Sample	% Sr	% K	% Ca	% Fe	% Ti	% Cu
LKD	2.10 ± 0.003	1.70 ± 0.01	86.62 ± 0.02	4.81 ± 0.01	0.44 ± 0.01	0.73 ± 0.01
BA	1.67 ± 0.02	8.68 ± 0.01	75.57 ± 0.02	5.03 ± 0.03	0.49 ± 0.01	1.03 ± 0.01

The elemental analysis omits major components aluminium and silicon, as they fall out of the dynamic range of the XRF analysis. Errors represent the standard deviation over triplicate measurements.

the samples has important implications for the environmental processing of these samples. These minerals will react with the acid deliquescent layer characteristic of processing during atmospheric transport, or less acidic media in water bodies, underground water, or pond reservoirs (Basu et al. 2009; Borgatta et al. 2016; Koshy and Singh 2016; Navea et al. 2017; Kim et al. 2020; Chowdhury et al. 2022). While both samples are thoroughly combusted, there are some indications of partially combusted fractions. This observation of partially combusted particles is in good agreement with the scanning electron microscopy (SEM) analysis, which shows amorphous rock-like particles in the samples. BA showed more rock-like structures than LKD, which shows some spherical particles formed during a highly efficient combustion process. We interpret this as an indication of BA having a slightly higher fraction of partially combusted particles, with most of the sample completely combusted.

The presence of mullite and calcite was confirmed via total attenuated reflectance–Fourier transform infrared spectra (ATR-FTIR) of samples, as shown in Fig. 2. As in the case of the XRD analysis (Fig. 1), FTIR spectra show similarities between LKD and BA. Both samples show a noticeable band around 1410 cm^{-1} which is characteristic of carbonates, in agreement with XRD data shown in Fig. 1. Carbonates and bicarbonates are important components in these samples as they react with acid and further breakdown particles, favouring the solubility by increasing surface area contact (Navea et al. 2010, 2017; Galhotra et al. 2009; Kim et al. 2020). Additionally, a sharp OH peak seen at 3647 cm^{-1} suggests isolated OH terminal groups in the dry samples. The bands centred at 1118 and 1042 cm^{-1} are assigned to vibrational absorption bands for the lattice stretching mode of Si–O (Borgatta et al. 2016; Navea et al. 2017; Galhotra et al. 2009), in agreement with the XRD bands of mullite and quartz reported in Fig. 1. While the composition of LKD and BA are similar, the band at 1042 cm^{-1} is only observed

in the LKD sample, indicating some small differences in the mineralogy of the samples. Finally, the sharp band centred at 877 cm^{-1} is assigned to deformation modes of Fe^{3+} within the aluminium silicate structure, $\delta(\text{FeAl-OH})$ (Navea et al. 2010, 2017; Borgatta et al. 2016). In general, elemental and chemical analysis data suggest that both samples are relatively similar in composition.

XPS compositional analysis revealed that the sample surface has significant amounts of calcium and oxygen. A marked difference was the presence of potassium in BA, in agreement with XRF analysis. Carbonates were detected in C 1s at 289.9 eV signifying a CaCO_3 structure (Usher et al. 2007). Traces of other elements, including sulfur, silicon, magnesium, and aluminium, were detected. Ultimately, XPS results suggest particle surfaces were dominated compositionally by calcium carbonates.

The surface areas for LKD and BA were found to be 6.3 ± 0.8 and $3.2 \pm 0.6\text{ m}^2\text{ g}^{-1}$, respectively. Both samples were sieved to select a maximum size of $35\text{ }\mu\text{m}$. Key information on specific surface area and total bulk iron content in each ash sample is summarised in Table 2.

Iron dissolution

As discussed in the Experimental section, two different combustion powder samples, LKD and BA, were used to determine iron dissolution into acidic media. Fig. 3 shows the fraction of Fe species dissolved from LKD and BA from pH 1.0 to 4.0, relative to the amount of iron (both Fe^{2+} and Fe^{3+}) as reported in Table 1.

While both combustion samples are relatively similar in mineralogy and particle size, the fraction of iron leached from BA was slightly lower than that for LKD. The fraction of total iron leached from LKD, as shown in Fig. 3, is roughly 15% at pH 1, compared to 12% for BA. At pH 2, the fraction of iron leached from both samples was statistically similar. Above pH 3, the solubility of Fe^{3+} from LKD approaches the limit of detection of the method (5 ppb), while Fe^{3+} leached from BA is also smaller but clearly above the limit of detection, with a slow solubility through the time of the experiment. Finally, Fig. 3 shows that the dissolution of iron into the aqueous phase takes place within 5–20 min of suspension at $\text{pH} < 2$, followed by passivation or slower dissolution. These two regimes are consistent with previous observations on iron dissolution from combustion particles in acidic media, where most available iron dissolves by a fast pathway (Borgatta et al. 2016; Kim et al. 2020).

This initial rate of dissolution, extracted from a linear fit from $t = 0$ to the passivation time (5–20 min) of the plots in Fig. 3, is measurable only at lower pH, under acidic conditions similar to the conditions found in the atmospheric aerosol deliquescent layer. The rate of iron dissolution for BA and LKD at low pH is similar to that observed for fly ashes. Considering mineralogy variations, iron dissolution from fly ash has been reported in a range of 5.1–0.17 at pH

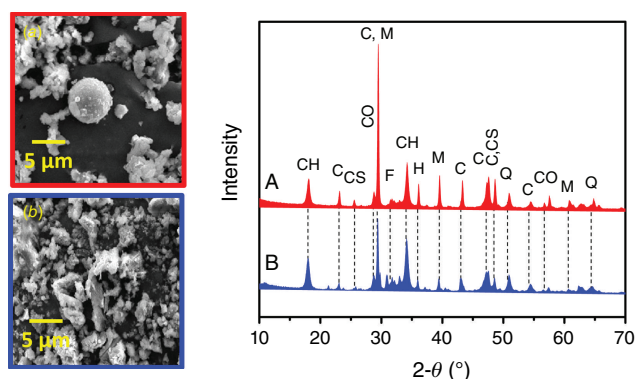


Fig. 1. Left: Representative micrographs of combustion samples. (a) Lime kiln dust (LKD); (b) bottom ash (BA). Right: X-ray diffraction characterisation of combustion samples. (a) LKD; (b) BA. XRD legend: C, calcium carbonate; CH, calcium hydroxide; CS, calcium silicate; Q, quartz; M, mullite; H, hematite/magnetite; F, feldspar.

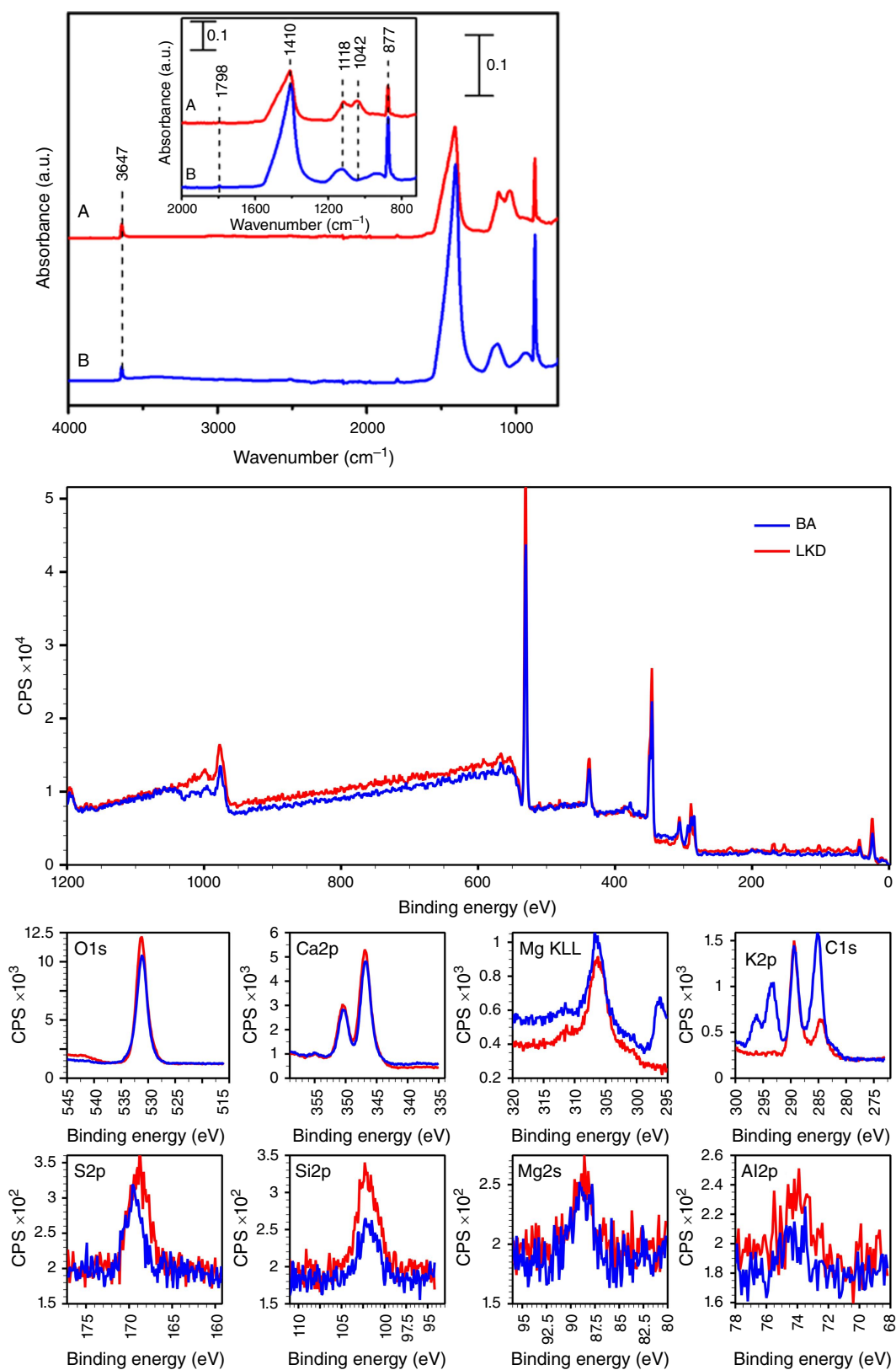


Fig. 2. (Caption on next page)

Fig. 2. (Top) Attenuated total reflection–Fourier transform infrared (ATR-FTIR) spectra showing LKD (a, red) and BA (b, blue) samples. The inset shows a magnified view of the spectroscopic region from 2000 to 750 cm^{-1} . (Bottom) Survey and high-resolution XPS spectra of LKD and BA sample surfaces. High-resolution XPS spectra show that the sample surface of both LKD and BA is primarily comprised of C, Ca, and O, whereas high-resolution spectra also show the presence of other elements, such as K, Si, Mg, and Al with a notable S 2p peak. A peak at 289.3 eV in the C 1s region is due to calcium carbonate, a combustion product in BA (Baltrusaitis et al. 2007).

Table 2. Iron content, specific surface area, and particle size in combustion particle samples: bottom ash (BA), lime kiln dust (LKD).

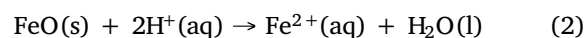
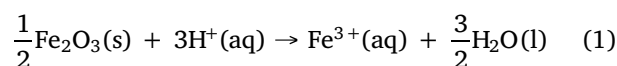
Sample	Total iron (mg g^{-1})	Surface area ($\text{m}^2 \text{g}^{-1}$)	Max particle size (μm)
BA	12.4 ± 0.5	3.2 ± 0.6	35
LKD	14.9 ± 0.8	6.3 ± 0.8	

1.0 and 6.0–0.203 at pH 2.0 (both rate ranges expressed in Fe ions $\text{cm}^{-3} \text{s}^{-1}$) (Borgatta et al. 2016; Kim et al. 2020). Both BA and LKD fall within this range. Furthermore, the total iron solubility remains statistically similar between pH 1.0 and 2.0, an effect also observed for the initial rate of iron dissolution from most fly ashes reported in the literature (Borgatta et al. 2016; Kim et al. 2020). As reported in mineral dissolution processes, surface iron species can have immediate contact with the acidic media and dissolve rapidly (Kim et al. 2020). As the pH increases, the rate of iron leach into aqueous media is not measurable, with the total iron dissolution to the aqueous phase decreasing to less than 2% of the total iron in the combustion sample. For both of the samples examined, the initial rate of dissolution at pH 1.0 and 2.0 is statistically similar. However, iron dissolution from LKD is faster than that of BA. At pH 3.0, BA shows a steady concentration of Fe^{3+} , corresponding to an average of only 2% of iron dissolved from the BA, with no measurable rate. On the other hand, the rate of dissolution for LKD at pH 3.0 is measurable, as shown in Table 3, but two orders of magnitude slower than the initial rates calculated at pH 1.0 and 2.0. Overall, the rate of iron dissolution from LKD and BA is comparable to those measured for fly ash samples (Kim et al. 2020). No rate was measurable at pH 4.0, with the iron concentration reaching passivation within 5 min of suspension time and concentrations nearing the limit of detection of the analysis method.

Fig. 4 shows the iron dissolution isotherms normalised to the BET surface area, as indicated in Table 1, for both LKD and BA relative to the time of suspension, at pH 1.0 to 4.0. Contrary to the observation of iron fraction dissolved, where LKD shows a slightly higher fraction of total iron dissolved compared to BA, the amount of dissolved Fe species per surface area was statistically equivalent for both samples at all examined pHs, indicating a correlation between Fe solubility and surface area, contrary to what has been observed in comparative studies of other combustion samples (Borgatta et al. 2016; Navea et al. 2017; Kim et al. 2020). Given the relative similarity in mineralogy between LKD and

BA, iron dissolution for these samples is a surface-controlled process. Specifically, when the chemical composition is relatively similar, the acid mobilisation of iron is the same when normalised by surface area, suggesting some dependency on surface properties. As in the case of iron fraction, nearly all iron partitions into the aqueous phase within the first 5–20 min of suspension. As the particle breaks down during the first dissolution time, with a concomitant increase in acid media contact with the iron-containing particle bulk, there is no significant increase in the iron concentration in the solution. This equilibrium stage suggests that most of the iron being mobilised is already on or near the surface of the particle (Marcotte et al. 2020). As the acidity of the media decreases, the particle fragmentation slows down, which is observed in the slow dissolution of iron at pH 3.0 for LKD.

Fig. 3 shows an increase in the fraction of dissolved total iron (Fe^{3+} and Fe^{2+}) with respect to suspension time for both combustion powder samples. Because suspensions take place in HCl, the main mechanism controlling the iron dissolution from the combustion particles is proton-promoted, as shown by Reactions (1) and (2) (Fu et al. 2010, 2012; Borgatta et al. 2016; Kim et al. 2020).



As suggested by a proton-promoted solubility mechanism, as pH increases, total iron ($\text{Fe}^{\text{total}} = \text{Fe}^{2+} + \text{Fe}^{3+}$) dissolution to the aqueous phase decreases. Most of the iron partitioned to the aqueous phase was Fe^{3+} , the oxidation state expected from highly oxidised samples, such as combustion particles. Given its low concentrations in solution, conclusions pertaining to Fe^{2+} are predominantly derived from absolute values rather than comparative assessments across varying pH levels. As the pH increases from 1.0 to 4.0, the concentration of dissolved Fe^{2+} , while lower than that of Fe^{3+} , fluctuates within a narrower range than the uncertainty of total iron concentration (including Fe^{2+} and Fe^{3+}). Therefore, Fe^{2+} concentration is bound by this uncertainty and remains statistically constant throughout the pH range examined. Since we conducted the dissolution experiments in the absence of light, dissolved Fe^{2+} must be the result of the dissolution of Fe^{2+} -containing solids within the ashes iron as reported in Table 2. This has significant biogeochemical implications as Fe^{2+} is more soluble than Fe^{3+} , providing trace iron even as the pH increases (Schoffman et al. 2016). Conversely, the yield of aqueous Fe^{3+} decreases as pH increases for both

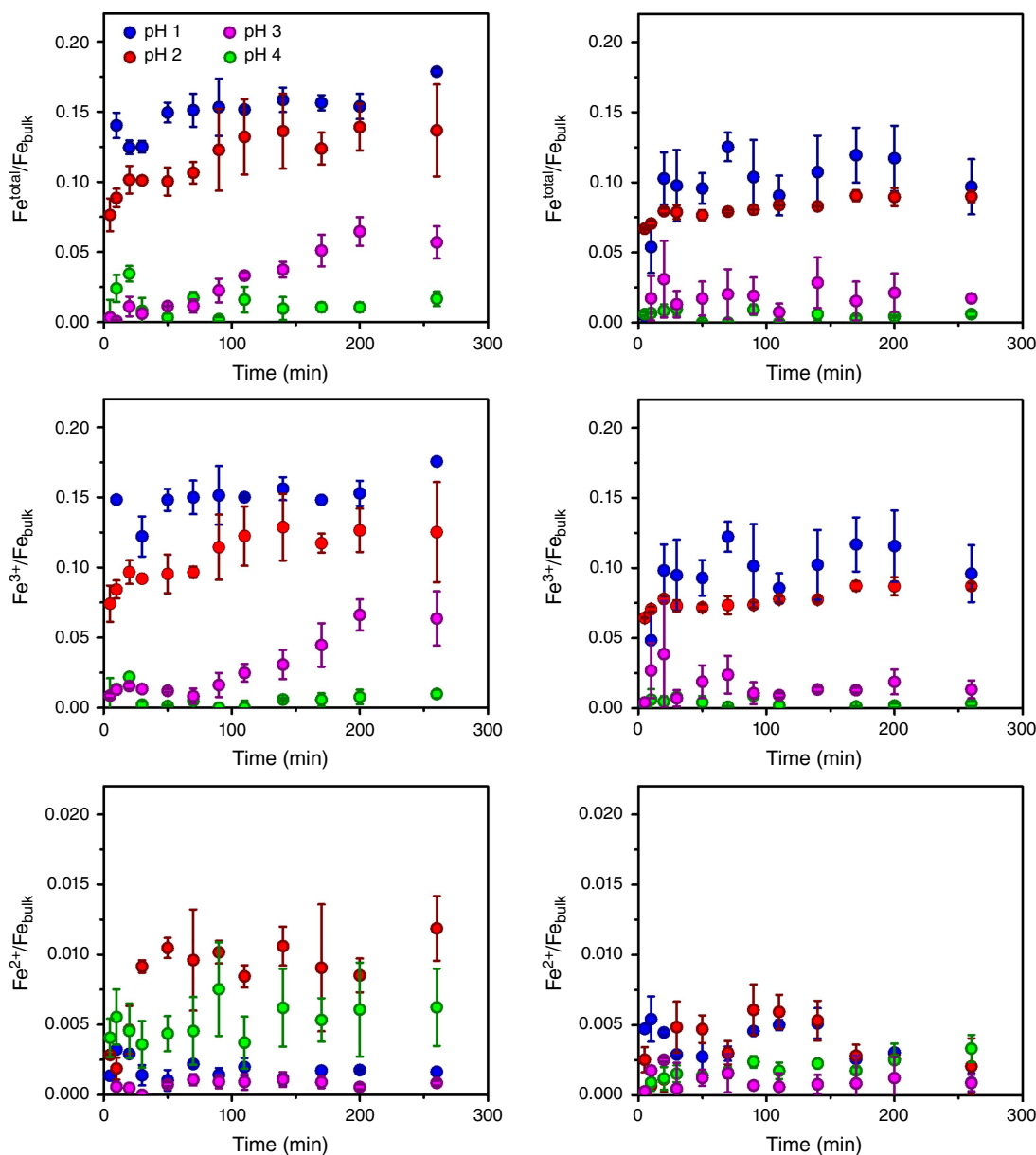


Fig. 3. Fraction of Fe species dissolved from combustion samples at pH = 1.0 (blue circles), 2.0 (red circles), 3.0 (purple circles), and 4.0 (green circles). Left panels: LKD; Right panels: BA. Top graphs represent total iron ($\text{Fe}^{\text{total}} = \text{Fe}^{2+} + \text{Fe}^{3+}$) leaching in HCl suspensions; middle graphs represent Fe^{3+} ; bottom graphs represent Fe^{2+} .

Table 3. Initial rate of the dissolution (v_i) of total iron ($\text{Fe}^{2+} + \text{Fe}^{3+}$) leached from BA and LKD suspensions at different pH.

Sample	v_i ($\times 10^{13}$ Fe ions $\text{cm}^{-3} \text{s}^{-1}$)			
	pH 1	pH 2	pH 3	pH 4
BA	2.9 ± 0.5	3.0 ± 0.3	n.o.	n.o.
LKD	3.8 ± 0.6	4.1 ± 0.5	0.083 ± 0.006	n.o.

n.o., not observed.

LKD and BA suspensions. While the yield of Fe^{3+} in solution after 100 min of suspension drops slightly from pH 1.0 to 2.0, there is a significant drop in Fe^{3+} concentrations at pH

higher than 3.0, with significantly lower fractions at pH 4.0. This decrease in Fe^{3+} concentration correlates well with the solubility of iron(III) oxide, hematite (Fe_2O_3), a component observed in the XRD analysis (Fig. 1) (Schwertmann 1991; Spokes and Jickells 1995). Thus, as pH increases the solubility of Fe_2O_3 decreases until it reaches a threshold above pH 3 (Losey *et al.* 2018; Freedman *et al.* 2019). In addition, Fe^{3+} dissolution requires a higher $\text{H}^+:\text{Fe}^{n+}$ ratio, at least three times higher for Fe^{3+} than that of Fe^{2+} , as shown by Reactions (1) and (2). Thus, according to the Le Chatelier principle, higher pH will tend to affect the solubility of Fe^{3+} more with the concomitant

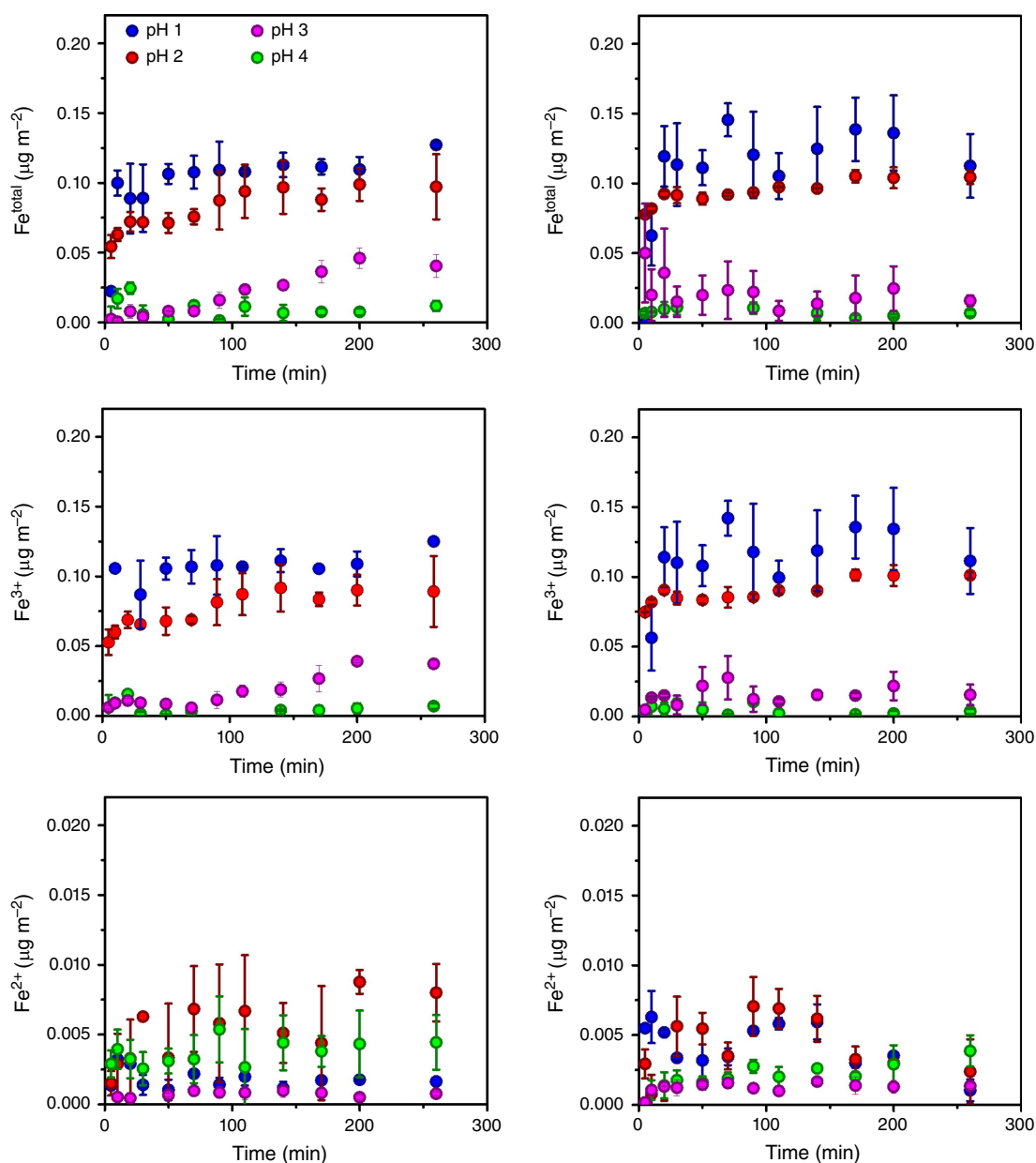


Fig. 4. Fe species dissolved from combustion samples normalised to BET surface area of LKD and BA at pH = 1.0 (blue circles), 2.0 (red circles), 3.0 (purple circles), and 4.0 (green circles). Left panels: LKD; Right panels: BA. Top graphs represent total iron ($\text{Fe}^{\text{total}} = \text{Fe}^{2+} + \text{Fe}^{3+}$) leaching in HCl suspensions; middle graphs represent Fe^{3+} ; bottom graphs represent Fe^{2+} .

drop in the fractional solubility of total iron from the combustion particles examined. In addition, the presence of carbonates, as shown by FTIR and XRD analysis, makes solubility more sensitive to pH, with protons dissolving structural CO_3^{2-} and HCO_3^- , with the concomitant weakening of the physical integrity of the combustion particles (Bargar *et al.* 2005; Navea *et al.* 2010; Borgatta *et al.* 2016; Kim *et al.* 2020). While the particles show mineralogical similarities, the difference in the solubility of iron between LKD and BA is likely linked to the bulk and surface abundance of Fe oxide

and Fe-containing aluminosilicates. As both FTIR and XPS analysis suggest (Fig. 2), the presence of Fe-substituted aluminosilicates may represent an important source of soluble Fe in combustion particles.

For every experiment, an equilibrium concentration of iron species was determined using the average iron concentration shown in Fig. 4 after the passivation time up to 260 min of suspension. Since a slow iron dissolution can take place, the passivation time was assumed to be 90 min for every experiment, ensuring that equilibrium

concentrations had been reached. In the case of LKD suspension at pH 3.0, characterised by a slow iron dissolution, equilibrium concentrations were calculated between 160 and 260 min. As shown in Fig. 5, a comparison between equilibrium concentrations of iron normalised by surface area shows statistically similar values for both BA and LKD at low pH. Because of the oxidation process, the overall mineralogy of these particles is similar, with iron speciation likely favouring Fe^{3+} . Thus, at a high concentration of H^+ , the surface area is the driving force of the iron dissolution to the aqueous phase, with the dissolution depending on the amount of surface OH terminal groups available to react, which are shown by the bands centred at 3647 and 877 cm^{-1} in the infrared spectra of both combustion samples, likely from the lattice structure of aluminosilicate structures, as suggested by the presence of Si and Al in the XPS analysis (Fig. 2) (Galhotra *et al.* 2009; Fu *et al.* 2012; Chen and Grassian 2013). These interactions between surface OH groups and the acidic media weaken surface structures and contribute to the mobilisation of iron into the aqueous phase (Zinder *et al.* 1986; Sulzberger *et al.* 1989; Remucal and Sedlak 2011; Ostaszewski *et al.* 2018; Drapanauskaite *et al.* 2021). As pH increases, these proton-driven processes become less prevalent. As a consequence, with the decrease in the concentration of H^+ , Reaction (1) yields lower concentrations of Fe^{3+} , with a more significant decrease in Fe^{3+} yield for BA than that for LKD. With a larger surface distribution and a larger amount of iron, LKD iron dissolution is still observable at pH 3.0; however, it slows down about fifty times compared to the rate of dissolution at pH 1.0 and 2.0. This effect is also dependent on the solubility of the metal oxide because the solubility of Fe_2O_3 decreases around pH 3.0 (Larsen and Vaida 2012). Conversely, for Fe^{2+} this effect is not observed, as the yield of the equilibrium concentration of

Fe^{2+} is statistically similar at all pH examined, as shown in Fig. 5 in the striped section of the bars.

As the pH increases beyond pH 3.0, the equilibrium concentrations of Fe^{3+} and Fe^{2+} become statistically similar for BA. For LKD, the equilibrium concentration of Fe^{3+} is only slightly higher than that for Fe^{2+} , as shown in Fig. 5 for pH 4.0 conditions. At pH 3.0 and 4.0, the small differences in the mineralogy and surface composition between the samples are responsible for this slight difference between them (Borgatta *et al.* 2016). Overall, there is approximately 20% less iron at pH 3 and 4.0 than that at pH 1.0 and 2.0 for Fe^{3+} and total Fe. Yet, for Fe^{2+} , the concentration of aqueous Fe^{2+} remains statistically similar at pH 1.0–4.0. This effect can be observed by the change in the speciation fraction of Fe^{2+} at equilibrium ($\alpha_{\text{Fe}^{2+}}$), calculated with Eqn 3,

$$\alpha_{\text{Fe}^{2+}} = \frac{[\text{Fe}^{2+}]_{\text{eq}}}{([\text{Fe}^{3+}]_{\text{eq}} + [\text{Fe}^{2+}]_{\text{eq}})} \quad (3)$$

As the pH increases, the total equilibrium concentration of iron decreases, but the fraction of bioavailable iron, while slowly increasing from pH 1.0 to pH 3.0, sharply increases above pH 3.0, reaching values where $\alpha_{\text{Fe}^{2+}} \approx \alpha_{\text{Fe}^{\text{tot}}}$. Overall, this indicates that while pH can have a significant effect on the solubility of iron, the relative speciation fraction of Fe^{2+} at equilibrium increases. This maintains the biogeochemical impact of the iron-containing particles over the acidic pH range examined, as Fe^{2+} solubility continues to provide dissolved iron.

Conclusions

Recent studies suggest that iron-containing aerosolised combustion particles can dissolve and mobilise iron faster than mineral dust aerosols under environmentally relevant conditions (Baldo *et al.* 2022). As an energy process by-product with little value, iron-containing combustion particles tend to accumulate and, despite containment efforts, occasionally partition into the environment, where they can contribute to Earth's iron mobility and budget. In particular, the smaller combustion particles used in this work ($< 35 \mu\text{m}$) are more susceptible to long range atmospheric transport. To better understand iron dissolution from these anthropogenic combustion particles, we carried out a comparative acidic iron dissolution of ash samples with relatively similar mineralogy, controlling for total iron content and specific surface area of the samples. The data presented herein show that the acidic iron solubility of samples with similar compositions has some dependency on particle composition and surface properties of the particles. The surface particle composition, such as OH surface terminal groups, and carbonate/bicarbonate content, is a driving force in iron dissolution that has been overlooked in climate and biogeochemical models (Al-Abadleh *et al.* 2022). The speciation of dissolved iron from the combustion particles examined is dominated by Fe^{3+} , as combustion

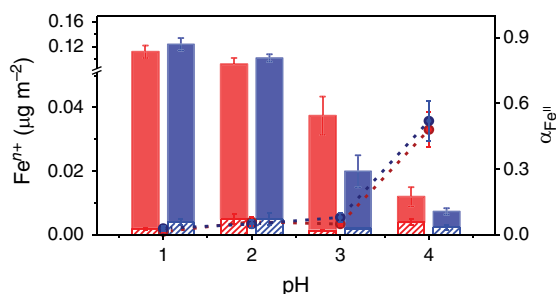


Fig. 5. Left axis: Average equilibrium concentrations of total iron ($\text{Fe}^{\text{total}} = \text{Fe}^{2+} + \text{Fe}^{3+}$) normalised by the surface area of LKD (red) and BA (blue). The solid section represents the average equilibrium concentrations of Fe^{3+} normalised by surface area, the striped section represents the average equilibrium concentration of Fe^{2+} normalised by surface area. Right axis: speciation fraction of Fe^{2+} ($\alpha_{\text{Fe}^{2+}}$) in equilibrium. The red dotted line and symbol represent LKD and the blue dotted line and symbol represent BA.

particles are highly oxidised. Thus, combustion particles dissolving in the aerosol deliquescent layer (pH 1.0 and 2.0) will primarily mobilise Fe^{3+} (Usher et al. 2003; Navea et al. 2010, 2017; Angle et al. 2021; Leonardi et al. 2020).

The relative steady concentration of Fe^{2+} across the pH examined suggests that its solubility in the aerosol deliquescent layer can be similar in acidic waters and ponds, where weak dissolved organic acids acidify the system. Compounds such as humic acid and fulvic acid are known reducing and photo-reducing agents, often found in soil and dissolved matter in rivers and lakes (Ricker et al. 2022; Mora Garcia et al. 2021). These acids have a pK_a between 4 and 6, allowing them to chelate and mobilise Fe^{2+} in environmental systems (Talbot et al. 1990; Borgatta and Navea 2015). In the atmospheric environment, where pH ranges from 1 to 3 (Ervens et al. 2004), larger amounts of iron can be mobilised from aerosolised combustion particles, with Fe^{3+} being the primary speciation of dissolved iron. However, this work shows that the contribution of dissolved Fe^{2+} tends to increase with pH for both combustion samples, suggesting that Fe^{2+} can continue to dissolve beyond atmospheric processing. While these results show the relevance of the acidic atmospheric processing on the solubility of iron from combustion particles, recent studies have shown that daylight can enhance solubility through photocatalytic processes, especially when semiconductor metal oxides are present in the particles (Fu et al. 2010, 2012; Mao et al. 2013; Hettiarachchi et al. 2018; Kim et al. 2020). Future studies should be conducted to determine if the photoinduced dissolution of iron from BA and LKD can open a pathway for further iron solubility and affect its speciation. Overall, this work shows that iron dissolution from LKD and BA is similar to that measured for fly ash, and is faster than iron dissolution from mineral dust aerosols (Borgatta et al. 2016; Baldo et al. 2022; Kim et al. 2020; Marcotte et al. 2020).

References

- Al-Abadleh HA (2015) Review of the bulk and surface chemistry of iron in atmospherically relevant systems containing humic-like substances. *RSC Advances* 5(57), 45785–45811. doi:10.1039/C5RA03132J
- Al-Abadleh H (2021) Aging of atmospheric aerosols and the role of iron in catalyzing brown carbon formation. *Environmental Science: Atmospheres* 1(6), 297–345. doi:10.1039/D1EA00038A
- Al-Abadleh H, Kubicki JD, Meskhidze N (2022) A perspective on iron (Fe) in the atmosphere: air quality, climate, and the ocean. *Environmental Science: Processes & Impacts* 25, 151–164. doi:10.1039/D2EM00176D
- Angle KJ, Crocker DR, Simpson RMC, Mayer KJ, Garofalo LA, Moore AN, Mora Garcia SL, Or VW, Srinivasan S, Farhan M, Sauer JS, Lee C, Pothier MA, Farmer DK, Martz TR, Bertram TH, Cappa CD, Prather KA, Grassian VH (2021) Acidity across the interface from the ocean surface to sea spray aerosol. *Proceedings of the National Academy of Sciences* 118(2), e2018397118. doi:10.1073/pnas.2018397118
- Arulrajah A, Mohammadinia A, D'Amico A, Horpibulsuk S (2017) Effect of lime kiln dust as an alternative binder in the stabilization of construction and demolition materials. *Construction and Building Materials* 152, 999–1007. doi:10.1016/j.conbuildmat.2017.07.070
- Baldo C, Ito A, Krom MD, Li W, Jones T, Drake N, Ignatyev K, Davidson N, Shi Z (2022) Iron from coal combustion particles dissolves much faster than mineral dust under simulated atmospheric acidic conditions. *Atmospheric Chemistry and Physics* 22(9), 6045–6066. doi:10.5194/acp-22-6045-2022
- Baltrusaitis J, Usher CR, Grassian VH (2007) Reactions of sulfur dioxide on calcium carbonate single crystal and particle surfaces at the adsorbed water carbonate interface. *Physical Chemistry Chemical Physics* 9(23), 3011–3024. doi:10.1039/b617697f
- Bargar JR, Kubicki JD, Reitmeier R, Davis JA (2005) ATR-FTIR spectroscopic characterization of coexisting carbonate surface complexes on hematite. *Geochimica et Cosmochimica Acta* 69(6), 1527–1542. doi:10.1016/j.gca.2004.08.002
- Basu M, Pande M, Bhadoria PBS, Mahapatra SC (2009) Potential fly-ash utilization in agriculture: a global review. *Progress in Natural Science* 19(10), 1173–1186. doi:10.1016/j.pnsc.2008.12.006
- Borcherding JA, Chen H, Caraballo JC, Baltrusaitis J, Pezzulo AA, Zabner J, Grassian VH, Comellas AP (2013) Coal Fly Ash Impairs Airway Antimicrobial Peptides and Increases Bacterial Growth. *PLoS One* 8(2), e57673. doi:10.1371/journal.pone.0057673
- Borgatta J, Navea JG (2015) Fate of Aqueous Iron Leached from Tropospheric Aerosols during Atmospheric Acidic Processing: Study of the Effect of Humic-Like Substances. *WIT Transactions on Ecology and the Environment* 198, 155–166.
- Borgatta J, Paskavitz A, Kim D, Navea JG (2016) Comparative evaluation of iron leach from different sources of fly ash under atmospherically relevant conditions. *Environmental Chemistry* 13(4), 902–912. doi:10.1071/EN16046
- Chen H, Grassian VH (2013) Iron Dissolution of Dust Source Materials during Simulated Acidic Processing: The Effect of Sulfuric, Acetic, and Oxalic Acids. *Environmental Science & Technology* 47(18), 10312–10321. doi:10.1021/es401285s
- Chen Y, Street J, Paytan A (2006) Comparison between pure-water- and seawater-soluble nutrient concentrations of aerosols from the Gulf of Aqaba. *Marine Chemistry* 101(1), 141–152. doi:10.1016/j.marchem.2006.02.002
- Chen H, Laskin A, Baltrusaitis J, Gorski CA, Scherer MM, Grassian VH (2012) Coal Fly Ash as a Source of Iron in Atmospheric Dust. *Environmental Science & Technology* 46(4), 2112–2120. doi:10.1021/es204102f
- Chowdhury A, Naz A, Chowdhury A (2022) Waste to resource: applicability of fly ash as landfill geoliner to control ground water pollution. *Materials Today: Proceedings* 60, 8–13. doi:10.1016/j.matpr.2021.10.367
- Chuang PY, Duvall RM, Shafer MM, Schauer JJ (2005) The origin of water soluble particulate iron in the Asian atmospheric outflow. *Geophysical Research Letters* 32(7), L07813. doi:10.1029/2004GL021946
- Drapanaukaitė D, Bunevičienė K, Repšienė R, Mazeika R, Navea J, Baltrusaitis J (2021) Physicochemical Characterization of Pelletized Lime Kiln Dust as Potential Liming Material for Acidic Soils. *Waste and Biomass Valorization* 12, 1267–1280. doi:10.1007/s12649-020-01107-0
- Drapanaukaitė D, Bunevičienė K, Repšienė R, Karčiauskienė D, Mažeika R, Baltrusaitis J (2022) The Effect of Pelletized Lime Kiln Dust Combined with Biomass Combustion Ash on Soil Properties and Plant Yield in a Three-Year Field Study. *Land* 11(4), 521. doi:10.3390/land11040521
- Ervens B, Feingold G, Frost GJ, Kreidenweis SM (2004) A modeling study of aqueous production of dicarboxylic acids: 1. Chemical pathways and speciated organic mass production. *Journal of Geophysical Research: Atmospheres* 109, D15205. doi:10.1029/2003JD004387
- Fairley N, Fernandez V, Richard-Plouet M, Guillot-Deudon C, Walton J, Smith E, Flahaut D, Greiner M, Biesinger M, Tougaard S, Morgan D, Baltrusaitis J (2021) Systematic and collaborative approach to problem solving using X-ray photoelectron spectroscopy. *Applied Surface Science Advances* 5, 100112. doi:10.1016/j.apsadv.2021.100112
- Freedman MA, Ott E-JE, Marak KE (2019) Role of pH in Aerosol Processes and Measurement Challenges. *The Journal of Physical Chemistry A* 123(7), 1275–1284. doi:10.1021/acs.jpca.8b10676
- Fu H, Cwiertny DM, Carmichael GR, Scherer MM, Grassian VH (2010) Photoreductive dissolution of Fe-containing mineral dust particles in acidic media. *Journal of Geophysical Research: Atmospheres* 115(D11), D11304. doi:10.1029/2009JD012702
- Fu H, Lin J, Shang G, Dong W, Grassian VH, Carmichael GR, Li Y, Chen J (2012) Solubility of Iron from Combustion Source Particles in

- Acidic Media Linked to Iron Speciation. *Environmental Science & Technology* 46(20), 11119–11127. doi:10.1021/es302558m
- Galhotra P, Navea JG, Larsen SC, Grassian VH (2009) Carbon dioxide ($C^{16}O_2$ and $C^{18}O_2$) adsorption in zeolite Y materials: effect of cation, adsorbed water and particle size. *Energy & Environmental Science* 2(4), 401–409. doi:10.1039/b814908a
- Haque ME (2013) Indian fly-ash: production and consumption scenario. *International Journal of Waste Resources* 3(22), 22–25. doi:10.12777/ijwr.3.1.2013.22-25
- Hettiarachchi E, Rubasinghe G (2020) Mechanistic Study on Iron Solubility in Atmospheric Mineral Dust Aerosol: Roles of Titanium, Dissolved Oxygen, and Solar Flux in Solutions Containing Different Acid Anions. *ACS Earth and Space Chemistry* 4, 101–111. doi:10.1021/acsearthspacechem.9b00280
- Hettiarachchi E, Reynolds RL, Goldstein HL, Moskowit B, Rubasinghe G (2018a) Iron dissolution and speciation in atmospheric mineral dust: Metal-metal synergistic and antagonistic effects. *Atmospheric Environment* 187, 417–423. doi:10.1016/j.atmosenv.2018.06.010
- Hettiarachchi E, Hurab O, Rubasinghe G (2018b) Atmospheric Processing and Iron Mobilization of Ilmenite: Iron-Containing Ternary Oxide in Mineral Dust Aerosol. *The Journal of Physical Chemistry A* 122(5), 1291–1302. doi:10.1021/acs.jpca.7b11320
- Hettiarachchi E, Reynolds RL, Goldstein HL, Moskowit B, Rubasinghe G (2019) Bioavailable iron production in airborne mineral dust: controls by chemical composition and solar flux. *Atmospheric Environment* 205, 90–102. doi:10.1016/j.atmosenv.2019.02.037
- Kabisch K, Hemmerling J (1982) 'Ponds and pools: oases in the landscape.' (Arco Publishing: New York, NY, USA)
- Kim D, Xiao Y, Karchere-Sun R, Richmond E, Ricker HM, Leonardi A, Navea JG (2020) Atmospheric processing of anthropogenic combustion particles: effects of acid media and solar flux on the iron mobility from fly ash. *ACS Earth and Space Chemistry* 4(5), 750–761. doi:10.1021/acsearthspacechem.0c00057
- Koshy N, Singh DN (2016) Fly ash zeolites for water treatment applications. *Journal of Environmental Chemical Engineering* 4(2), 1460–1472. doi:10.1016/j.jece.2016.02.002
- Larsen MC, Vaida V (2012) Near Infrared photochemistry of pyruvic acid in aqueous solution. *The Journal of Physical Chemistry A* 116, 5840–5846. doi:10.1021/jp2087972
- Leonardi A, Ricker HM, Gale AG, Ball BT, Odbadrakh TT, Shields GC, Navea JG (2020) Particle formation and surface processes on atmospheric aerosols: a review of applied quantum chemical calculations. *International Journal of Quantum Chemistry* 120, e26350. doi:10.1002/qua.26350
- Losey DJ, Sihvonen SK, Veghte DP, Chong E, Freedman MA (2018) Acidic processing of fly ash: chemical characterization, morphology, and immersion freezing. *Environmental Science: Processes & Impacts* 20(11), 1581–1592. doi:10.1039/c8em00319j
- Luo C, Mahowald N, Bond T, Chuang PY, Artaxo P, Siefert R, Chen Y, Schauer J (2008) Combustion iron distribution and deposition. *Global Biogeochemical Cycles* 22, GB1012. doi:10.1029/2007GB002964
- Mahowald NM, Engelstaedter S, Luo C, Sealy A, Artaxo P, Benitez-Nelson C, Bonnet S, Chen Y, Chuang PY, Cohen DD, Dulac F, Herut B, Johansen AM, Kubilay N, Losno R, Maenhaut W, Paytan A, Prospero JM, Shank LM, Siefert RL (2009) Atmospheric Iron Deposition: Global Distribution, Variability, and Human Perturbations. *Annual Review of Marine Science* 1(1), 245–278. doi:10.1146/annurev.marine.010908.163727
- Mao J, Fan S, Jacob DJ, Travis KR (2013) Radical loss in the atmosphere from Cu-Fe redox coupling in aerosols. *Atmospheric Chemistry and Physics* 13(2), 509–519. doi:10.5194/acp-13-509-2013
- Marcotte AR, Anbar AD, Majestic BJ, Herckes P (2020) Mineral Dust and Iron Solubility: Effects of Composition, Particle Size, and Surface Area. *Atmosphere* 11(5), 533. doi:10.3390/atmos11050533
- Matsui H, Mahowald NM, Moteki N, Hamilton DS, Ohata S, Yoshida A, Koike M, Scanza RA, Flanner MG (2018) Anthropogenic combustion iron as a complex climate forcer. *Nature Communications* 9(1), 1593. doi:10.1038/s41467-018-03997-0
- Moore JK, Doney SC, Glover DM, Fung IY (2001) Iron cycling and nutrient-limitation patterns in surface waters of the World Ocean. *Deep Sea Research Part II: Topical Studies in Oceanography* 49(1), 463–507. doi:10.1016/S0967-0645(01)00109-6
- Moore CM, Mills MM, Arrigo KR, Berman-Frank I, Bopp L, Boyd PW, Galbraith ED, Geider RJ, Guieu C, Jaccard SL, Jickells TD, La Roche J, Lenton TM, Mahowald NM, Marañón E, Marinov I, Moore JK, Nakatsuka T, Oeschles A, Saito MA, Thingstad TF, Tsuda A, Ulloa O (2013) Processes and patterns of oceanic nutrient limitation. *Nature Geoscience* 6(9), 701–710. doi:10.1038/ngeo1765
- Mora Garcia SL, Pandit s, Navea JG, Grassian VH (2021) Nitrous Acid (HONO) Formation from the Irradiation of Aqueous Nitrate Solutions in the Presence of Marine Chromophoric Dissolved Organic Matter: Comparison to Other Organic Photosensitizers. *ACS Earth and Space Chemistry* 5(11), 3056–3064. doi:10.1021/acsearthspacechem.1c00292
- Mueller SF, Mallard JW, Mao Q, Shaw SL (2013) Fugitive particulate emission factors for dry fly ash disposal. *Journal of the Air & Waste Management Association* 63(7), 806–818. doi:10.1080/10962247.2013.795201
- Navea JG, Grassian VH (2017) Photochemistry of Atmospheric Particles. In 'Encyclopedia of Interfacial Chemistry: Surface Science and Electrochemistry'. (Eds K Wandelt, K Kolasinski) pp. 553–562. (Elsevier: Oxford, UK)
- Navea JG, Chen h, Huang M, Carmichel GR, Grassian VH (2010) A comparative evaluation of water uptake on several mineral dust sources. *Environ. Chem.* 7(2), 162–170. doi:10.1071/EN09122
- Navea JG, Isomond E, Stortini T, Greenspan J (2017) Water Adsorption Isotherms on Fly Ash from Several Sources. *Langmuir* 33(39), 10161–10171. doi:10.1021/acs.langmuir.7b02028
- Nowinski P, Hodge VF, Gerstenberger S (2012) Application of field portable X-ray fluorescence to the analysis of desert varnish samples in areas affected by coal-fired power plants. *Environmental Chemistry* 9(4), 379–388. doi:10.1071/EN11139
- Ojha K, Pradhan NC, Samanta AN (2004) Zeolite from fly ash: synthesis and characterization. *Bulletin of Materials Science* 27(6), 555–564. doi:10.1007/BF02707285
- Ostaszewski CJ, Stuart NM, Lesko DMB, Kim D, Lueckheide MJ, Navea JG (2018) Effects of Coadsorbed Water on the Heterogeneous Photochemistry of Nitrates Adsorbed on TiO_2 . *The Journal of Physical Chemistry A* 122(31), 6360–6371. doi:10.1021/acs.jpca.8b04979
- Pinedo-González P, Hawco NJ, Bundy RM, Armbrust EV, Follows MJ, Cael BB, White AE, Ferrón S, Karl DM, John SG (2020) Anthropogenic Asian aerosols provide Fe to the North Pacific Ocean. *Proceedings of the National Academy of Sciences* 117(45), 27862–27868. doi:10.1073/pnas.2010315117
- Ramanathan V, Crutzen PJ, Kiehl JT, Rosenfeld D (2001) Aerosols, Climate, and the Hydrological Cycle. *Science* 294(5549), 2119–2124. doi:10.1126/science.1064034
- Remucal CK, Sedlak DL (2011) The Role of Iron Coordination in the Production of Reactive Oxidants from Ferrous Iron Oxidation by Oxygen and Hydrogen Peroxide. In 'Aquatic Redox Chemistry'. (Eds PG Tratnyek, TJ Grundl, SB Haderlein) pp. 177–197. (American Chemical Society: WA, USA)
- Ricker HM, Leonardi A, Navea JG (2022) Reduction and Photoreduction of NO_2 in Humic Acid Films as a Source of HONO, ClNO, N_2O , NO_x , and Organic Nitrogen. *ACS Earth and Space Chemistry* 6(12), 3066–3077. doi:10.1021/acsearthspacechem.2c00282
- Rubasinghe G, Lentz RW, Scherer MM, Grassian VH (2010) Simulated atmospheric processing of iron oxyhydroxide minerals at low pH: roles of particle size and acid anion in iron dissolution. *Proceedings of the National Academy of Sciences* 107(15), 6628–6633. doi:10.1073/pnas.0910809107
- Schoffman H, Lis H, Shaked Y, Keren N (2016) Iron-Nutrient Interactions within Phytoplankton. *Frontiers in Plant Science* 7, 1223. doi:10.3389/fpls.2016.01223
- Schroter AW, Crusius J, Sholkovitz ER, Bostick BC (2009) Iron solubility driven by speciation in dust sources to the ocean. *Nature Geoscience* 2(5), 337–340. doi:10.1038/ngeo501
- Schwertmann U (1991) Solubility and dissolution of iron oxides. *Plant and Soil* 130(1), 1–25. doi:10.1007/BF00011851
- Spokes LJ, Jickells TD (1995) Factors controlling the solubility of aerosol trace metals in the atmosphere and on mixing into seawater. *Aquat. Geochem.* 1, 355–374. doi:10.1007/BF00702739
- Sulzberger B, Suter D, Siffert C, Banwart S, Stumm W (1989) Dissolution of $Fe(III)(hydr)oxides$ in natural waters; laboratory assessment on the kinetics controlled by surface coordination. *Marine Chemistry* 28(1), 127–144. doi:10.1016/0304-4203(89)90191-6
- Talbot RW, Andreae MO, Berresheim H, Jacob DJ, Beecher KM (1990) Sources and sinks of formic, acetic, and pyruvic acids over central

- Amazonia: 2. Wet season. *Journal of Geophysical Research: Atmospheres* **95**, 16799–16811. doi:10.1029/JD095iD10p16799
- Usher CR, Michel AE, Grassian VH (2003) Reactions on mineral dust. *Chemical Reviews* **103**(12), 4883–4940. doi:10.1021/cr020657y
- Usher CR, Baltrusaitis J, Grassian VH (2007) Spatially Resolved Product Formation in the Reaction of Formic Acid with Calcium Carbonate (1014): The Role of Step Density and Adsorbed Water-Assisted Ion Mobility. *Langmuir* **23**(13), 7039–7045. doi:10.1021/la062866+
- Vassilev SV, Baxter D, Andersen LK, Vassileva CG (2013) An overview of the composition and application of biomass ash.: Part 2. Potential utilisation, technological and ecological advantages and challenges. *Fuel* **105**, 19–39. doi:10.1016/j.fuel.2012.10.001
- Zinder B, Furrer G, Stumm W (1986) The coordination chemistry of weathering: II. Dissolution of Fe(III) oxides. *Geochimica et Cosmochimica Acta* **50**(9), 1861–1869. doi:10.1016/0016-7037(86)90244-9

Data availability. Data for this study can be accessed in the Center for Aerosol Impacts on Chemistry of the Environment (CAICE) University of California San Diego Library Digital Collections (<https://doi.org/10.6075/J0QJ7HGM>).

Conflicts of interest. The authors declare no conflicts of interest.

Declaration of funding. This work is supported by the National Science Foundation through the 995 NSF Center for Aerosol Impacts on the Chemistry of the Environment, a Center for Chemical Innovation CHE-1801971 (JN) and NSF Environmental Chemical Sciences program CHE 1710120 (JB).

Author affiliations

^AChemistry Department, Skidmore College, Saratoga Springs, NY 12866-1632, USA.

^BDepartment of Chemical and Biomolecular Engineering, Lehigh University, B336 Iacocca Hall, 111 Research Drive, Bethlehem, PA 18015, USA.

^CInstitute of Agriculture, Lithuanian Research Centre for Agriculture and Forestry, Kedainiai dist., Instituto av. 1, Akademija LT-58344, Lithuania.